*Article*

# ROBI': A Prototype Mobile Manipulator for Agricultural Applications

**Luca Bascetta \*, Marco Baur and Giambattista Gruosso**

Politecnico di Milano, Dipartimento di Elettronica, Informazione e Bioingegneria, Piazza Leonardo da Vinci 32, 20133 Milano, Italy; marco.baur@polimi.it (M.B.); giambattista.gruosso@polimi.it (G.G.)

\* Correspondence: luca.bascetta@polimi.it; Tel.: +39-02-2399-3440

**Abstract:** The design of ROBI', a prototype mobile manipulator for agricultural applications devised following low-cost, low-weight, simplicity, flexibility and modularity requirements, is presented in this work. The mechanical design and the selection of the main components of the motion control system, including sensors and in-wheel motors, is described. The kinematic and dynamic models of the robot are also derived, with the aim to support the design of a trajectory tracking system and to make a preliminary assessment of the design choices, as well. Finally, two simulations, one specifically related to a realistic trajectory in an agricultural field, show the validity of these choices.

**Keywords:** off-road mobile manipulator design; in-wheel motors; agricultural robotics

## 1. Introduction

Precision agriculture practices are the most effective way to significantly reduce the negative impact of farming on the environment, due to over-application of chemicals, while still producing enough food to satisfy a growing demand. Indeed, turning traditional farming into precision farming not only lowers the chemical load in food and the environment, but also improves farmers' profits and harvest yields, giving farmers a return on their investments [1]. The introduction of advanced sensing capabilities allows monitoring at the plant level, spotting problems before they spread. Furthermore, introducing farming robots, chemicals can be applied with honeybee precision; pesticides and fungicides can be used only when needed and in the smallest necessary amount, or even be substituted by less impacting techniques (e.g., mechanical instead of chemical thinning, biological control instead of chemical pesticides). In brief, the introduction of advanced perception capabilities (i.e., high-tech sensors) and action capabilities (i.e., robotic platforms) brings a leading-edge technological approach to farming, allowing for observing, measuring and acting.

The revolution represented by precision farming and by the introduction of robotic platforms entails, however, the solution of many different scientific and technological challenges related to navigation and manipulation capabilities. Among the scientific challenges, we can mention perception skills, like mapping, localization and obstacle detection. Considering, for example, navigation in a hilly environment characterized by substantial terrain roughness, an algorithm to perform accurate 3D reconstruction and localization [2,3] of the mobile platform plays an important role. Two other important challenges that have to be mentioned are related to planning and control. Consider a complex off-road environment; the planning algorithm [4,5] should be able to devise a path that is feasible, i.e., compatible with the platform kinematic and dynamic constraints, and safe with respect to terrain roughness and slope. The trajectory tracking controller [6] has to fulfill similar requirements.

To support the development of such a multidisciplinary research, the availability of accurate models for dynamic analysis, control system design and validation [7] and for perception algorithm testing and software validation [8] is of utmost importance. This, however, represents only the first

and preliminary validation step and, in any case, cannot substitute an experimental test campaign. For this reason, the availability of prototype off-road mobile manipulators is an important step to support the research on agricultural robotics.

This paper describes the design and realization of a mobile manipulator for agricultural applications that aims at being characterized by low cost, low weight and having a simple mechanical design. In other words, a prototype that can be easily built, without requiring complex machining, from a mounting kit, so that it can be easily distributed as an open source project.

The robotics literature is full of different works dealing with the design and development of robotic platforms for agricultural applications, starting from the pioneering work in [9] on the design of a systems engineering method to evaluate the performance of an agricultural robot. Focusing now on the last decade, we can mention works devoted to the design of mobile manipulators for specific tasks, like white asparagus harvesting [10], tomato harvesting [11,12], weed and pest control [13], or considering the development of platforms for different field operations, but lacking an arm, like the Thorvald platform [14], or focused on the development of arms or grippers optimized for specific tasks [15–18], or taking into account other modular, flexible and low-cost solutions, as the ones described in [19–23].

About mobile manipulators, which are the matter of this work, it must be noticed that the solutions proposed in [10–12] are all task specific. Moreover, the solution proposed in [12] is based on an omni-directional platform that is not suitable for off-road navigation, while the robot described in [11] is only for greenhouse use.

Furthermore, the platforms designed for a general agricultural task do not include an arm and differ from the one here proposed because they are based on more complex and expensive mechanical solutions [13,14,22], or they are not modular and adaptable [21–23], or they are focused on farmer assistance, but not suitable for autonomous operation [19].

Finally, in the last two years, interesting review papers, investigating the research effort, developments and innovation in agricultural robots for field operations, have been published [24–27]. The interested reader is referred to these papers for a more detailed analysis of the state-of-the-art in agricultural robotics.

The paper is organized as follows. Section 2 describes the design of the experimental platform, including the chassis, in-wheel motors, power system and robotic arms. Section 3 introduces a kinematic and a dynamic model of the mobile platform. Section 4 reports the experimental characterization of in-wheel motors and two simulations aiming at verifying the design choices. Section 5 concludes the paper describing future developments of the ROBI' platform.

## 2. Design and Realization

ROBI' (Figure 1) is a prototype small-sized mobile manipulator for agricultural applications, whose aim is to support the development and testing of innovative perception and control algorithms. As such a small vehicle, equipped with a couple of half a meter long arms, can operate on many different crops, ranging from vineyards to herbaceous plants, the main geometrical features of the robot, i.e., ground clearance, track, wheelbase, should be easily adaptable. Considering, as an example, the case of ridge sowing, the height of the ridge can vary between 20 and 40 cm and the row distance between 90 and 120 cm. To accomplish this task, a mobile base should have a clearance of about 50 cm, and a track of 100 cm is required.

Besides the adaptability of the geometrical characteristics, the design choices were driven by the following requirements:

- low cost, in order to have a research prototype that can be easily realized in multiple examples to study fleet management algorithms;
- low weight, in order to increase, as much as possible, the batteries' discharge time and, thus, the mission length;

- simple mechanical design, so that the robot can be easily built, without requiring complex machining, from a mounting kit (and thus, easily distributed as an open source project).

This section describes the main design choices related to the development of the chassis, the engine, the power systems and the robotic arms.



**Figure 1.** ROBI'mobile manipulator.

*2.1. Chassis*

The chassis has been designed mainly focusing on:

- lightness, to reduce the amount of energy needed to drive the robot;
- flexibility, to easily adapt the robot geometrical configuration keeping the same components.

The chassis is made of ITEM$^{\circledR}$ aluminum bars, characterized by a lightweight, but strong section. It has been designed in such a way that the front and rear bars represent a slide rail for the two lateral bars, at which the wheels are linked, so that the wheelbase can be easily changed. Moreover, these four bars together form a rectangular rigid linkage at which four short bars, supporting the wheels, can be connected through four rotational joints, that allow changing the robot track and ground clearance.

Figure 2 depicts three among all of the possible chassis configurations: track, width and clearance can be varied in the ranges reported in Table 1.

Finally, at present, the robot features rigid suspensions. Shock absorbers, however, can be easily introduced without altering the chassis design.

Considering that the robot is equipped with two arms, located in the front part, and that the power system is constituted by car batteries located in the rear part, the maximum allowed longitudinal/lateral terrain slopes can be easily derived. Assuming a maximum front payload, including arm weight, of 15 kg, in the most critical configuration, i.e., minimum track and wheelbase and maximum ground clearance, rollover is prevented up to the case of a longitudinal or lateral slope of 45°.

(**a**)                                                              (**b**)



(**c**)
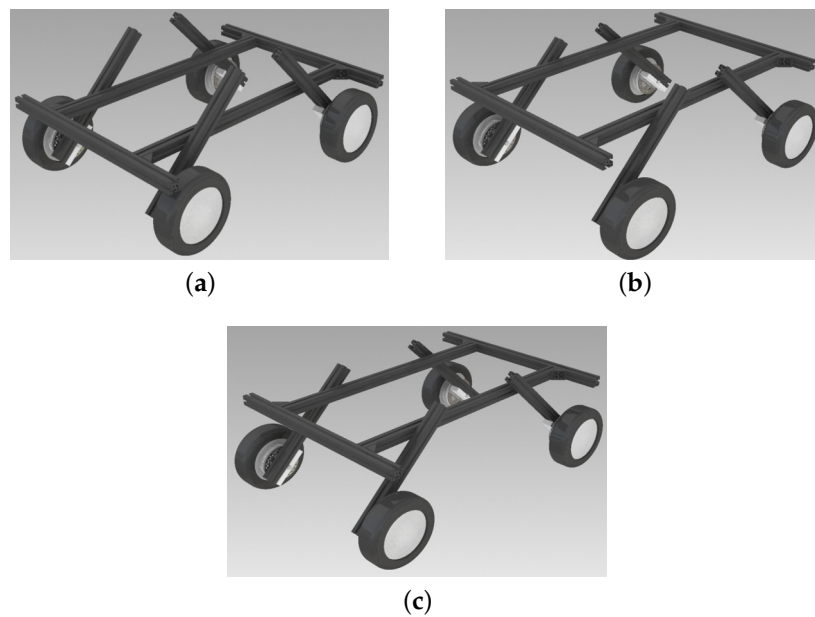
**Figure 2.** Some examples of chassis configurations. (**a**) Ground clearance of 250 mm; (**b**) track of 850 mm; (**c**) wheelbase of 900 mm.

**Table 1.** Range of variation of the main chassis geometrical characteristics.

| | |
|---|---|
| Ground clearance | $[0.25, 0.35]$ m |
| Track | $[0.75, 1.2]$ m |
| Wheelbase | $[0.6, 1]$ m |

### 2.2. In-Wheel Motors

ROBI' is powered by four in-wheel electric AC brushless motors. Table 2 reports the motor electrical and mechanical characteristics as given by the manufacturer.

**Table 2.** HUB10GL in-wheel motor main characteristics.

| | |
|---|---|
| Motor mass | 3.5 kg |
| Motor and tire mass | 5.7 kg |
| Power | 500 W |
| Voltage | 36 V |
| Maximum speed | 1350 rpm |
| Maximum operating voltage | 36 V |
| Tire diameter | 10 in |

In-wheel motors have many advantages with respect to a classical electrical powertrain constituted by one or two electric motors and a suitable drivetrain. First of all, with in-wheel motors, no transmission is required, making the mechanical design of the vehicle easier and more reliable, reducing the weight, increasing the amount of space available over the chassis for a payload and under it to improve ground clearance and avoiding components sticking out that can be damaged, or damage the environment, in the case of impacts. Furthermore, the vehicle can be easily equipped with four independent driving wheels that allow increasing the maneuverability, even without introducing an Ackermann kinematics that is characterized by a far more complex mechanical design and excessive realization costs, and open the way to the development of innovative control algorithms for the stability control of the vehicle on sloping and/or slippery terrains.

On the other hand, in-wheel motors measuring motor position and speed, which are both required to set up a current and a velocity controller, respectively, are more complex, due to the lack of a rotating axis at the chassis connection. As a matter of fact, an encoder can be mounted on the wheel rim at the expense, however, of a more complex mechanical design, required to create a rigid connection between the encoder stator and the chassis. Moreover, doing it in this way, the sensor is very close to the ground and, thus, exposed to potential impacts with rocks or other obstacles in the environment, as well as to dust and debris.

To overcome this problem, a belt transmission, which allows driving a rotating encoder mounted on top of the suspension arm, has been designed. Thanks to this transmission, encoders can be housed inside the chassis, preventing damages caused by accidental impacts and dust (Figure 3).



**Figure 3.** Encoder transmission.

The transmission is composed of two toothed pulleys and a timing belt, in order to avoid slippage and hence errors in the measurement of position and velocity. In order to comply with tight space constraints and keep the cost down, the pulleys have been designed with a 3D CAD software, featuring a 6 mm-wide T metric profile [28] and 3D printed on PLA plastic. Two of the printed pulleys are shown in Figure 4a.

Considering that the only torque transmitted by the two pulleys is due to bearing and belt friction, the design and the chosen polymer are appropriate to resist mechanical stress. However, a further FEM stress analysis (Figure 4b) has been performed considering the effect of a 10 Kg radial, tightening and pulling load, in order to verify the structural resistance and introduce a safety factor.

Another important advantage related to the introduction of the transmission is that it allows adopting lower resolution position sensors, again contributing to cost reduction. The diameter of the two pulleys (the bigger one mounted on the wheel, the smaller on the encoder axis) has been selected, taking into account the tight space constraints and the standard belt profiles, in such a way that the ratio is equal to 4.6. This design choice allows one to have a good position resolution even using encoders with no more than 512 lines.

The belt size has been then selected accordingly, considering a distance between the wheel and encoder axis of 300 mm and a width of 6 mm.
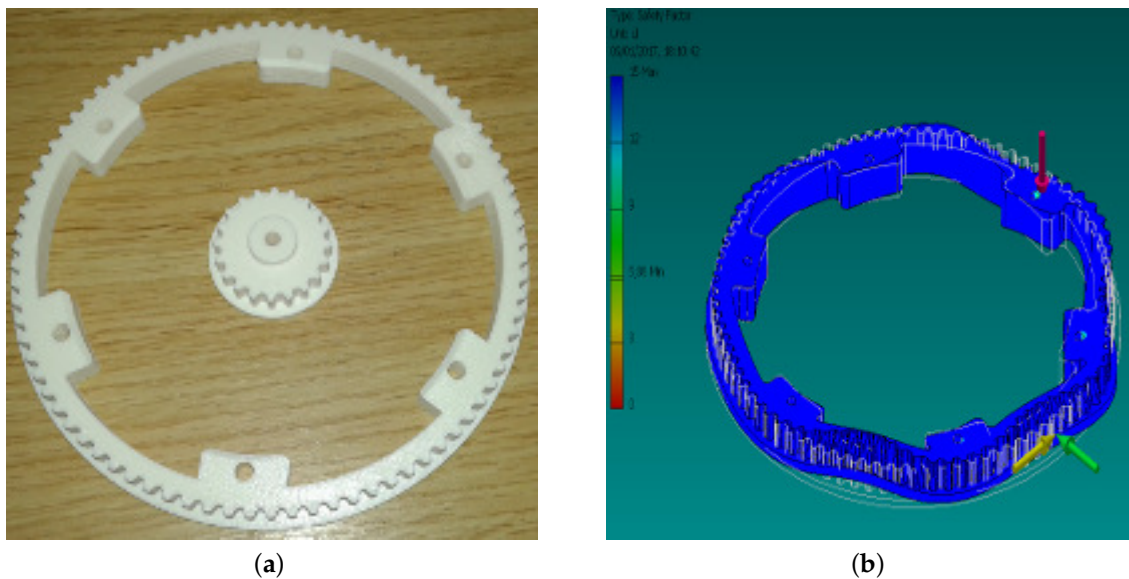
**Figure 4.** Encoder belt drivetrain pulleys. (**a**) 3D printed pulleys; (**b**) FEM analysis performed on the bigger pulley.

As the position measurement devices, ORBIS, a prototype encoder manufactured by RLS (Komenda, Slovenia, http://www.rls.si), has been selected. Though being a low-cost sensor, this encoder is characterized by a sensitivity of $\pm 0.3°$ and a resolution of 14 bit. Moreover, another peculiar characteristic of this device, making it particularly suitable for this application, is that there is no mechanical connection between the stator and the rotor (as the motion is transmitted from the encoder axis to the measuring electronics exploiting the magnetic effect), eliminating thus the risk of disk damages due to mechanical vibrations and shocks, which frequently happen when standard encoders are used in off-road vehicles.

Finally, each in-wheel motor is controlled using a suitable electronic board, whose hardware has been designed taking inspiration by an open source brushless motor control project [29] and will be adapted in order to support the coordination and synchronization of the four motors. The board (Figure 5) is an electronic motor speed controller, which consists mainly of an STM32F405 microcontroller and DRV8302 MOSFET drivers from Texas Instruments. The input power can be from 8–60 V, and the board can handle a continuous current up to 50 A. It has an input for Hall effect sensors, and it allows CAN (Controller Area Network) communication, SPI (Serial Peripheral Interface) which is used for the encoder, USART (Universal Synchronous/Asynchronous Receiver/Transmitter) and USB (Universal Serial Bus).
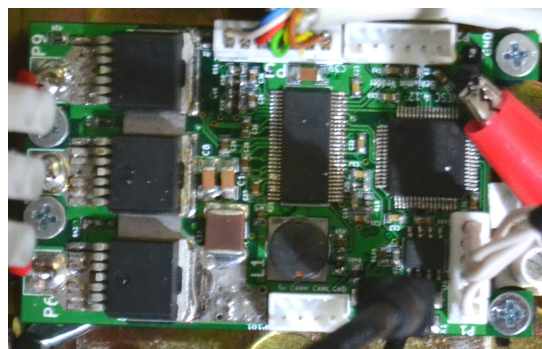


**Figure 5.** The motor control board.

As part of the experimental development, a suitable equipment to test the hardware (Figure 6), the control software and the encoder on a small motor has been designed and realized, as well. The test equipment consists of a platform to which the motor control board is attached, connected to the ORBIS encoder, to the motor and the Hall effect sensors. The platform is assembled so that the shaft of the motor, which is equipped with the encoder magnet, is aligned with the ORBIS encoder. The motor main wires pass through three current and voltage sensors, which are attached to a small oscilloscope for waveform analysis. The motor control board is connected via USB to a computer for data analysis and debugging.
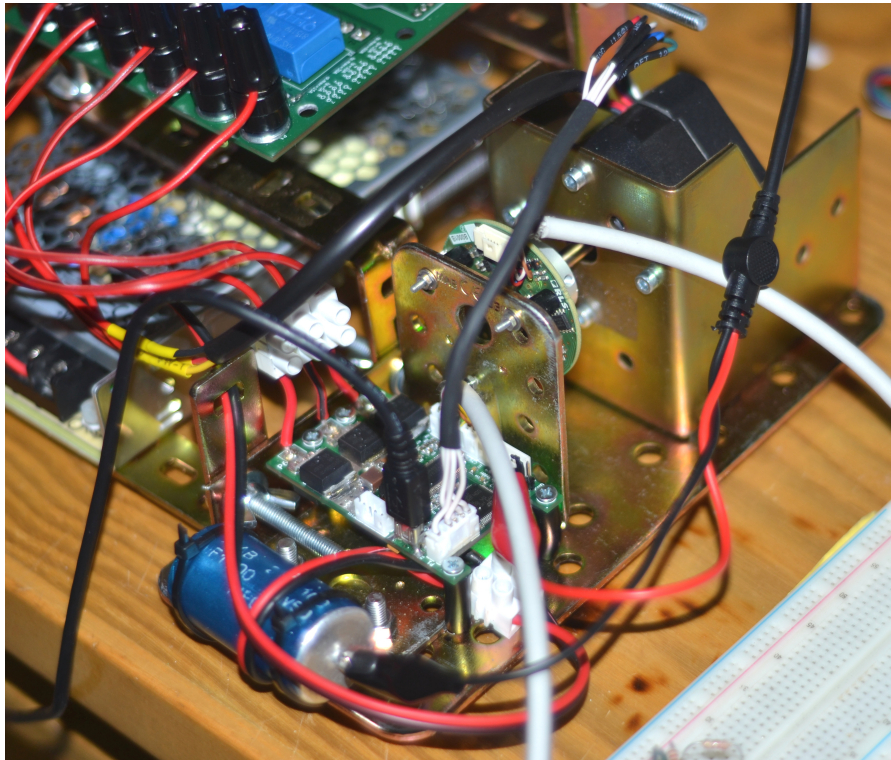


**Figure 6.** The equipment used to test the motor, encoder and control board.

*2.3. Power System*

The energy to motors and electronic boards is supplied by three 12 V lead acid deep charge batteries. Battery characteristics are reported in Table 3. This kind of battery was preferred to lithium ion ones, mainly for cost and reliability issues. Further experimental studies will be performed in the future collecting consumption data in different terrains and executing different tasks in order to compare the available battery technologies and determine the best one even in terms of discharge time.

**Table 3.** Battery main characteristics.

| | |
|---|---|
| Manufacturer | FIAM |
| Model | FGC22703 |
| Type | sealed lead acid |
| Voltage | 12 V |
| Capacity | 27 Ah |

## 2.4. Robotic Arms

In order to keep the robot open to different agricultural tasks, a two-arm configuration has been selected. At this stage, only a preliminary design has been performed, aimed at defining working space, motor power and positioning on the rover.

The main requirements in the selection of the manipulators are related to weight reduction, modularity, workspace size, ease of relocation and low cost. Standard commercial components, which allow one to set up a robot fulfilling all of the previous requirements, are manufactured by CrustCrawler Robotics (Modesto, CA, USA, http://www.crustcrawler.com). In order to satisfy workspace requirements and simplify the control problem, two six-d.o.f. anthropomorphic arms with a spherical wrist have been designed.

Thanks to the modularity of the CrustCrawler products, the design of the mechanical structure can be decoupled from the selection of motor powers, at least assuming that arm weight will not change significantly with respect to load weight and increasing arm length. Furthermore, different arm lengths can be adopted using producer's products, or custom arms can be easily designed and manufactured using rapid prototyping techniques.

An analysis of the typical tasks that the robot will be used for, considering the maximum platform height, as well, suggests to design two arms, each one characterized by four standard links with a length of 40 cm (Figure 7).



**Figure 7.** A 3D rendering of the mobile robot with two CrustCrawler manipulators.

On the other hand, to select joint motors, an estimate of the required torque has been performed. First of all, a maximum payload of 2 kg, including gripper and end effector sensing devices, has been considered, allowing for manipulation of small objects and visual inspection, even with heavy sensors. Then, the resistance torques at each joint have been computed as:

$$\tau_{r,j} = m_{payload} g d_{payload,j} + \sum_{i=1}^{6} m_i d_{i,j} \tag{1}$$

where $m_{payload}$ is the maximum payload mass, $m_i$ the mass of the $i$-th link and $d_{payload,j}$, $d_{i,j}$ are the distances from the payload to the $j$-th joint and from the $i$-th link center of gravity to the $j$-th joint, respectively. Finally, joint motors have been selected in such a way that:

$$\tau_{m,j} \geq 1.1\tau_{r,j} \qquad j = 1, \ldots, 6 \tag{2}$$

where $\tau_{m,j}$ is the nominal torque of the $j$-th joint motor.

Table 4 reports a list of standard Dynamixel (Lake Forest, CA, USA, http://www.robotis.us) servomotors that satisfy the previous constraints.

**Table 4.** Manipulator joint servomotors.

| Joint | Servomotor Model | Nominal Torque (Nm) |
|:-----:|:----------------:|:-------------------:|
| 0 | MX/RX-64 | 7.3 |
| 1 | MX/RX-28 | 3.1 |
| 2 | MX/RX-64 | 7.3 |
| 3 | MX/RX-64 dual axis | 14.6 |
| 4 | AX12A | 1.5 |
| 5 | AX18A | 1.8 |

## 3. Modeling a Skid Steering Robot

This Section introduces the tools required to derive a kinematic and dynamic model of a skid steering platform. This model is then used to support the design and preliminary testing of a trajectory tracking controller and to validate the design choices.

To support the derivation of the kinematic and dynamic models, we introduce a local reference frame $(x, y, z)$ centered in the robot center of gravity and a global inertial reference frame $(X, Y, Z)$ (Figure 8).
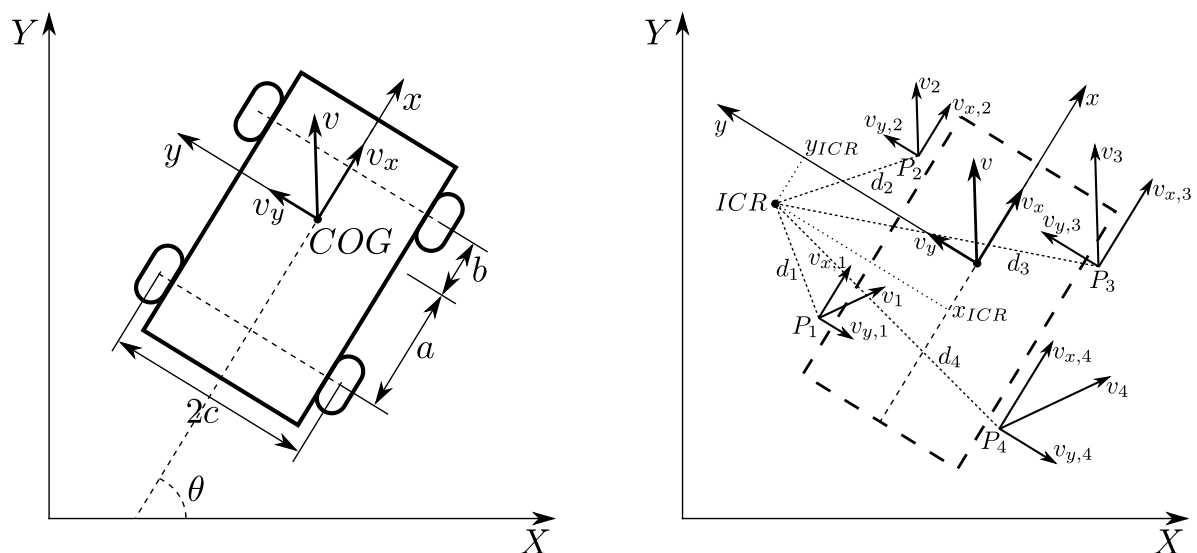


**Figure 8.** Robot (**left** image) and wheel (**right** image) reference frames ($Z$ and $z$ axis pointing towards the reader).

### 3.1. Kinematic Model

Considering pure rolling, the velocity of the $i$-th wheel (Figure 8), with respect to the local robot frame, can be expressed as:

$$v_{x,i} = r\omega_i \qquad v_{y,i} = 0 \tag{3}$$

where $r$, $\omega_i$ are the wheel radius (assuming all of the wheels have the same radius) and angular velocity, respectively, and $v_{x,i}$, $v_{y,i}$ the longitudinal and lateral velocity.

Assuming that the robot is following a curvilinear path in the $XY$-plane, at each time instant, an Instantaneous Center of Rotation (ICR) can be defined (Figure 8), whose position with respect to the local frame is denoted by $(x_{ICR}, y_{ICR})$. On the other hand, $d_{x,i}$ and $d_{y,i}$ represent the projection, on the local $x$ and $y$ axis, of the vectors $d_i$ connecting the ICR to the $i$-th wheel contact point $P_i$ and can be computed as follows:

$$d_{x,1} = d_{x,4} = -x_{ICR} - a \tag{4}$$

$$d_{x,2} = d_{x,3} = -x_{ICR} + b \tag{5}$$

$$d_{y,1} = d_{y,2} = -y_{ICR} + c \tag{6}$$

$$d_{y,3} = d_{y,4} = -y_{ICR} - c \tag{7}$$

where $2c$ is the wheel track and $a$, $b$ are the distances from the center of gravity to rear and front axle, respectively (Figure 8).

If the motion of the robot along the curvilinear path is characterized by an angular velocity $\dot{\theta}$ with respect to the $z$ axis, the following kinematic relations hold:

$$-\frac{v_{x,i}}{d_{y,i}} = \frac{v_{y,i}}{d_{x,i}} = \frac{v_x}{y_{ICR}} = -\frac{v_y}{x_{ICR}} = \dot{\theta} \tag{8}$$

where $v_x$ and $v_y$ are the projections of the robot velocity $v$ on the local frame.

From Relation (8), a set of constraints on the wheel velocities follows:

$$v_{x,1} = v_{x,2} \qquad v_{x,3} = v_{x,4} \qquad v_{y,1} = v_{y,4} \qquad v_{y,2} = v_{y,3} \tag{9}$$

from which we derive:

$$\omega_L = \omega_1 = \omega_2 \qquad \omega_R = \omega_3 = \omega_4 \tag{10}$$

where $\omega_L$ and $\omega_R$ are the angular velocities of the left and right wheels, respectively.

Thanks to Equation (8), we can relate $\omega_L$, $\omega_R$ to $v_x$, $v_y$ as follows:

$$\begin{bmatrix} \omega_L \\ \omega_R \end{bmatrix} = \frac{1}{r} \begin{bmatrix} 1 & \dfrac{c}{x_{ICR}} \\ 1 & -\dfrac{c}{x_{ICR}} \end{bmatrix} \begin{bmatrix} v_x \\ v_y \end{bmatrix} \tag{11}$$

Finally, summing and subtracting the two equations in (11), we obtain a relation between the robot linear and angular velocity and the wheel velocities:

$$\begin{bmatrix} v_x \\ \dot{\theta} \end{bmatrix} = \frac{r}{2c} \begin{bmatrix} c & c \\ -1 & 1 \end{bmatrix} \begin{bmatrix} \omega_L \\ \omega_R \end{bmatrix} \tag{12}$$

and the inverse one:

$$\begin{bmatrix} \omega_L \\ \omega_R \end{bmatrix} = \frac{1}{r} \begin{bmatrix} 1 & -c \\ 1 & c \end{bmatrix} \begin{bmatrix} v_x \\ \dot{\theta} \end{bmatrix} \tag{13}$$

Equations (12) and (13) can be now rewritten introducing left and right longitudinal slip, which are defined as follows:

$$\varepsilon_L = \frac{r\omega_L - v_L}{r\omega_L} \qquad \varepsilon_R = \frac{r\omega_R - v_R}{r\omega_R} \tag{14}$$

where $v_L = v_{x,1} = v_{x,2}$ and $v_R = v_{x,3} = v_{x,4}$, as follows:

$$\begin{bmatrix} v_x \\ \dot{\theta} \end{bmatrix} = \frac{r}{2c} \begin{bmatrix} (1-\varepsilon_L)c & (1-\varepsilon_R)c \\ \varepsilon_L - 1 & 1 - \varepsilon_R \end{bmatrix} \begin{bmatrix} \omega_L \\ \omega_R \end{bmatrix} \tag{15}$$

and:

$$\begin{bmatrix} \omega_L \\ \omega_R \end{bmatrix} = \frac{1}{r(1-\varepsilon_R)(1-\varepsilon_L)} \begin{bmatrix} 1-\varepsilon_R & -(1-\varepsilon_R)c \\ 1-\varepsilon_L & (1-\varepsilon_L)c \end{bmatrix} \begin{bmatrix} v_x \\ \dot{\theta} \end{bmatrix} \tag{16}$$

To complete the robot kinematics, we must multiply Equation (12) or (15) by the rotation matrix that aligns the robot local reference frame to the global reference frame, obtaining, for the more general case of Equation (15):

$$\dot{\mathbf{q}} = \mathbf{B}\,(\mathbf{q}) \begin{bmatrix} \omega_L \\ \omega_R \end{bmatrix} \tag{17}$$

where $\mathbf{q} = \begin{bmatrix} X & Y & \theta \end{bmatrix}^T$, $\theta$ being the robot heading, and:

$$\mathbf{B}\,(\mathbf{q}) = \frac{r}{2c} \begin{bmatrix} \cos(\theta) & 0 \\ \sin(\theta) & 0 \\ 0 & 1 \end{bmatrix} \begin{bmatrix} (1-\varepsilon_L)c & (1-\varepsilon_R)c \\ \varepsilon_L - 1 & 1 - \varepsilon_R \end{bmatrix} \tag{18}$$

### 3.2. Dynamic Model

Considering that the motion of a skid steering robot is strongly related to the wheel slip effect, in order to have an accurate simulation of the system, a dynamic model, able to describe the wheel-ground interaction, is required.

Moreover, thanks to the small size and weight of the robot and the stiffness of the suspension system, roll and pitch motion can be neglected. On the other side, it is important to model the front/rear and left/right load transfers, due to lateral/longitudinal accelerations or to ground slope, that affect the load distribution on the wheels and thus ground friction. Accordingly, wheel load is computed using a steady-state approximation, in which the contributions of lateral and longitudinal accelerations, taking the slope of the terrain into account, are added to the static load distribution:

$$F_z^{f,l} = F_z^{f,static} - \Delta F_z^{y,f} - \Delta F_z^x \tag{19}$$

$$F_z^{f,r} = F_z^{f,static} + \Delta F_z^{y,f} - \Delta F_z^x \tag{20}$$

$$F_z^{r,l} = F_z^{r,static} - \Delta F_z^{y,r} + \Delta F_z^x \tag{21}$$

$$F_z^{r,r} = F_z^{r,static} + \Delta F_z^{y,r} + \Delta F_z^x \tag{22}$$

where:

$$F_z^{f,static} = \frac{m g_z a}{2l} \qquad F_z^{r,static} = \frac{m g_z b}{2l} \tag{23}$$

and:

$$\Delta F_z^{y,f} = \frac{mha}{2lc}\, a_y \qquad \Delta F_z^{y,r} = \frac{mhb}{2lc}\, a_y \qquad \Delta F_z^x = \frac{mh}{2l}\, a_x \tag{24}$$

with $m$ the mass of the vehicle, $a$ and $b$ the distance of the center of gravity from the rear and front axle, respectively, $g_z$ the component of the gravity acceleration vector along the $z$ axis of the local frame, $l$ the vehicle wheelbase ($l = a + b$), $c$ the vehicle track, $h$ the height of the center of gravity and $a_y / a_x$

the lateral/longitudinal acceleration resulting from vehicle dynamics and ground slope, respectively, and defined as follows:

$$a_x = \dot{v}_x + g_x \tag{25}$$

$$a_y = \dot{v}_y + g_y \tag{26}$$

In the previous equations, $g_x$, $g_y$ and $g_z$ refer to the components of the gravity acceleration vector $g$ expressed in the vehicle local reference frame, which are computed as follows [30]:

$$\begin{bmatrix} g_x \\ g_y \\ g_z \end{bmatrix} = R_X^{-1}(\phi) \ R_Y^{-1}(\gamma) \ R_Z^{-1}(\theta) \begin{bmatrix} g_X \\ g_Y \\ g_Z \end{bmatrix} \tag{27}$$

where $\phi$ and $\gamma$ are the terrain slopes considered as clockwise rotations around the global $X$ and $Y$ axis, respectively, and $\theta$ is the vehicle attitude angle, i.e., its orientation as a clockwise rotation along the global $Z$ axis (note that, $g_X = g_Y = 0$ and $g_Z = -9.81 \, \text{m/s}^2$). $R_X$, $R_Y$ and $R_Z$ are the rotation matrices representing elementary rotations with respect to the $X$, $Y$ and $Z$ axis of the global reference frame, respectively.

The vehicle attitude angle $\theta$ is computed by integrating the vehicle yaw rate $\dot{\theta}$, which is determined, along with vehicle longitudinal and lateral speed $v_x$ and $v_y$, using the equations of motion. These equations are derived starting from the dynamic equilibria expressed in the global reference frame as:

$$m\ddot{X} = F_X \tag{28}$$

$$m\ddot{Y} = F_Y \tag{29}$$

$$J_z\ddot{\theta} = M_Z \tag{30}$$

where $F_X$, $F_Y$ represent the sum of the forces acting along the $X$- and $Y$ axis, $M_Z$ the yaw moment, $J_z$ the moment of inertia with respect to the $z$ axis and $m$ the robot mass.

The previous equations can be projected onto the local reference frame, obtaining:

$$m\left(\dot{v}_x - \dot{\theta}v_y\right) = F_{x_{L_{front}}} + F_{x_{R_{front}}} + F_{x_{L_{rear}}} + F_{x_{R_{rear}}} \tag{31}$$

$$m\left(\dot{v}_y + \dot{\theta}v_x\right) = F_{y_{L_{front}}} + F_{y_{R_{front}}} + F_{y_{L_{rear}}} + F_{y_{R_{rear}}} \tag{32}$$

$$\begin{aligned} J_z\ddot{\theta} &= \left(F_{x_{R_{front}}} + F_{x_{R_{rear}}}\right)c + \left(F_{y_{L_{front}}} + F_{y_{R_{front}}}\right)a \\ &- \left(F_{x_{L_{front}}} + F_{x_{L_{rear}}}\right)c - \left(F_{y_{L_{rear}}} + F_{y_{R_{rear}}}\right)b \end{aligned} \tag{33}$$

where $F_{x_{**}}$, $F_{y_{**}}$ are the wheel-ground interaction forces.

An accurate description of these forces, considering either rigid and deformable terrains, is out of the scope of this work. For this reason, they are here modeled using a variation of the Pacejka magic formula [31,32]. This variation was introduced to consider that nominal robot speed is rather small compared to nominal car speed and to simplify the relation neglecting non-relevant effects, like camber. Under these assumptions, the longitudinal and lateral forces of a general wheel can be expressed as:

$$F_x = \begin{cases} C_\sigma \sigma & \sigma < 1 \\ \mu_x F_z & \sigma \geq 1 \end{cases} \qquad F_y = \begin{cases} -C_\alpha \alpha & \alpha < 1 \\ -\mu_y F_z & \alpha \geq 1 \end{cases} \tag{34}$$

where $\sigma$, $\alpha$ are the longitudinal and lateral slip, respectively, $C_\sigma$, $C_\alpha$ are the cornering stiffness, $\mu_x$, $\mu_y$ the longitudinal and later friction that characterize the specific terrain and $F_z$ is the vertical load on the wheel, including the static load and load transfer.

It must be noticed, however, that the longitudinal and lateral forces are independent only when the wheel generates forces in a single direction. Otherwise, the relation between the two forces can be approximated as follows:

$$\frac{F_x^2}{F_{x_0}^2} + \frac{F_y^2}{F_{y_0}^2} = 1 \tag{35}$$

where $F_{x_0}$ is the maximum longitudinal force, corresponding to $\alpha = 0$, and $F_{y_0}$ is the force acting on the wheel when $F_x = 0$.

Finally, to close the model, we define the longitudinal and lateral slip of a general wheel as:

$$\sigma = \frac{r\omega - v}{v} \tag{36}$$

and:

$$\alpha_L = \begin{cases} \arctan\left(\dfrac{v_y + \dot{\theta}b}{v_x - \dot{\theta}c}\right) & \text{front wheels} \\ \arctan\left(\dfrac{v_y - \dot{\theta}a}{v_x - \dot{\theta}c}\right) & \text{right wheels} \end{cases} \qquad \alpha_R = \begin{cases} \arctan\left(\dfrac{v_y + \dot{\theta}b}{v_x + \dot{\theta}c}\right) & \text{front wheels} \\ \arctan\left(\dfrac{v_y - \dot{\theta}a}{v_x + \dot{\theta}c}\right) & \text{right wheels} \end{cases} \tag{37}$$

where $v$ is the vehicle velocity, and the angular velocity $\omega$ of each wheel can be computed using the equilibrium:

$$J_{z_w}\dot{\omega} = \tau_m - rF_x \tag{38}$$

where $J_{z_w}$ is the wheel moment of inertia and $\tau_m$ is the torque generated by the in-wheel motor.

## 4. Simulation Results

This section presents the results of some simulations that allow one to verify the design and, in particular, the torque and power consumption of the selected in-wheel motors, as well as the battery operating time. First of all, the following activities have been performed:

- standard motion control systems, based on cascaded velocity/current loops, have been designed (see Table 5 for the main characteristics);
- numerical values of the mechanical parameters required to simulate the model have been derived from the nominal values reported in Section 2 and from the CAD model;
- numerical values of the electrical parameters of the in-wheel motors have been experimentally identified, as will be described in the following part of this section;
- numerical values describing wheel-ground interaction forces have been derived from standard models [32] of motor-scooter tires (as the in-wheel motors used are usually manufactured for electric motor-scooter);
- as the design of a trajectory tracker controller is out of the scope of this work, robot trajectories used in this section have been planned using the kinematic model.

The section is organized as follows. First of all, the procedure used to identify the in-wheel motor parameters is described. Then, two simulations are introduced: one considering a line path that shows the behavior of the system in a very simple situation; the second one based on a more realistic agricultural scenario, demonstrates the effectiveness of the design choices.

**Table 5.** Main characteristics of the motion control system.

|  | Rise Time ms | Settling Time ms | Overshoot % |
|---|---|---|---|
| Current loop | 1.0 | 6.0 | 11.10 |
| Speed loop | 9.4 | 93.4 | 6.97 |

### 4.1. In-Wheel Motor Parameter Identification

Different experimental tests have been performed on the in-wheel motors in order to estimate the main motor parameters.

First of all, no-load tests at different velocities have been executed moving the wheel with a high power continuous current motor and measuring phase voltages. Though the manufacturer declares that the in-wheel motor is a DC brushless motor, tests reveal a perfectly sinusoidal back-EMF voltage. For this reason, motor speed has been estimated directly from the frequency of the back-EMF voltages. The results of different tests are reported in Table 6, showing a very good accuracy in the estimate of the magnetic flux and the back-EMF constant.

**Table 6.** Results of no-load tests.

| Frequency Hz | Voltage V | $K_E$ Vs/rad | Speed rpm | $K_E$ V/rpm | Magnetic Flux Wb |
|---|---|---|---|---|---|
| 10.076 | 2.284 | 0.3608 | 60.456 | 0.0378 | 0.0208 |
| 20.515 | 4.655 | 0.3611 | 123.09 | 0.0378 | 0.0209 |
| 30.717 | 6.965 | 0.3609 | 184.302 | 0.0378 | 0.0208 |
| 40.839 | 9.256 | 0.3607 | 245.034 | 0.0378 | 0.0208 |
| 51.598 | 11.689 | 0.3605 | 309.588 | 0.0378 | 0.0208 |
| 61.991 | 14.036 | 0.3604 | 371.946 | 0.0377 | 0.0208 |
| 72.559 | 16.426 | 0.3603 | 435.354 | 0.0377 | 0.0208 |
| 83.063 | 18.774 | 0.3597 | 498.378 | 0.0377 | 0.0208 |
| 93.679 | 21.164 | 0.3596 | 562.074 | 0.0377 | 0.0208 |

Then, a set of short circuit tests at different frequencies has been executed in order to estimate the phase inductance. However, due to the uncertainty on the phase resistance, whose nominal value is $80\,m\Omega$, the phase inductance cannot be accurately estimated. To increase the estimation accuracy, a resistor, with a nominal resistance of $0.47\,\Omega$ (definitely bigger than the phase resistance) was added to each phase. The accurate values of the resistance ($R_{ext}$) and inductance ($L_{ext}$) of these resistors at different frequencies have been estimated using an impedance meter (see Table 7). The phase resistance and inductance have been then estimated from current and back-EMF measurements, using the following relation:

$$\frac{E_{phase}(\omega)}{I(\omega)} = \sqrt{\left(R_{phase} + R_{ext}\right)^2 + \omega^2 \left(L_{phase} + L_{ext}\right)^2} \tag{39}$$

where $E_{phase}(\omega)$, $I(\omega)$ are the phase back-EMF and current at frequency $\omega$, $R_{phase}$, $L_{phase}$ are the phase resistance and inductance and $R_{ext}$, $L_{ext}$ are the added resistor resistance and inductance. The results of different tests are reported in Table 7, showing a good accuracy in the estimate of resistance/inductance of the added resistor and of the motor phase resistance/inductance, as well.

**Table 7.** Results of load tests (currents and voltages are the amplitude of the first harmonic).

| Frequency Hz | Current Arms | Voltage Vrms | Back-EMF V | $R_{ext}$ $\Omega$ | $L_{ext}$ mH | $R_{phase}$ $\Omega$ | $L_{phase}$ mH |
|---|---|---|---|---|---|---|---|
| 14.424 | 3.27 | 1.62 | 1.88 | 0.495 | 0.137 | 0.080 | 0.313 |
| 25.719 | 5.85 | 2.87 | 3.35 | 0.491 | 0.046 | 0.080 | 0.351 |
| 33.088 | 7.53 | 3.67 | 4.32 | 0.487 | 0.033 | 0.080 | 0.396 |
| 45.662 | 10.33 | 5.03 | 5.96 | 0.486 | 0.025 | 0.080 | 0.370 |
| 60.336 | 13.54 | 6.55 | 7.87 | 0.484 | 0.021 | 0.080 | 0.365 |

### 4.2. A Rectilinear Trajectory

The first simulation concerns a rectilinear trajectory with a length of 175 m, taking 20 s (Figure 9). This preliminary test aims at showing that, at least in a simple situation, the selection of in-wheel motors and battery system fulfills the required specifications.
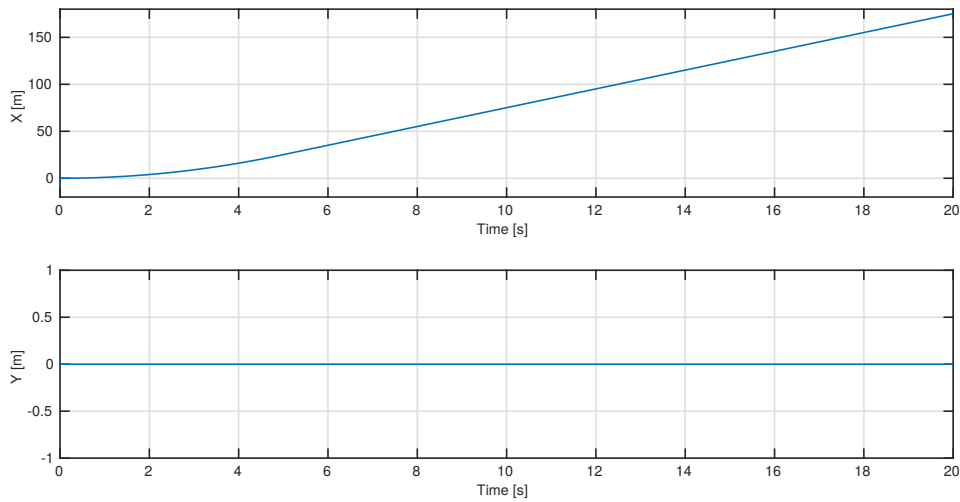


**Figure 9.** *x* and *y* robot trajectory.

First, Figure 10a shows that the required motor torque for the two left wheels and the two right wheels during the acceleration and the constant velocity parts of the trajectory (Figure 10b) are below the maximum and nominal motor torque. As expected, this implies that motor voltages and currents (Figure 11) are below the maximum values, as well.

Finally, Figure 12 shows the motor power of rear motors and the battery energy consumption. The energy required to execute a rectilinear trajectory at the conditions considered in this simulation is approximately 4.08 Wh, 1.54 Wh during the acceleration phase and 2.54 Wh during the constant velocity phase. Considering that the battery pack has a capacity of 972 Wh, the vehicle autonomy in this situation is approximately 1 h and 36 min.



(**a**)

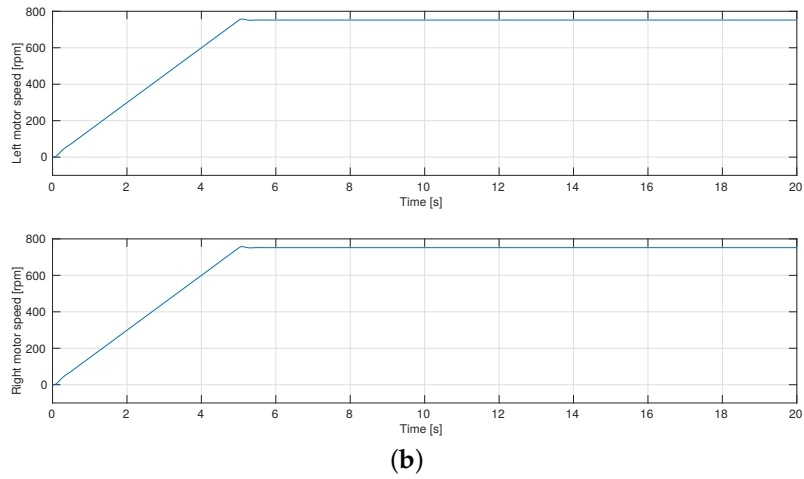**Figure 10.** *Cont.*

**(b)**
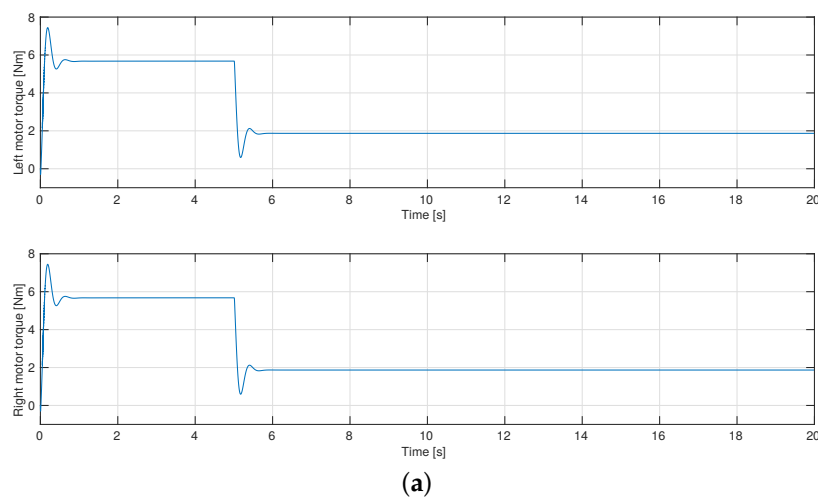
**Figure 10.** Torque and speed of the rear left and right in-wheel motors. (**a**) Motor torque; (**b**) motor speed.
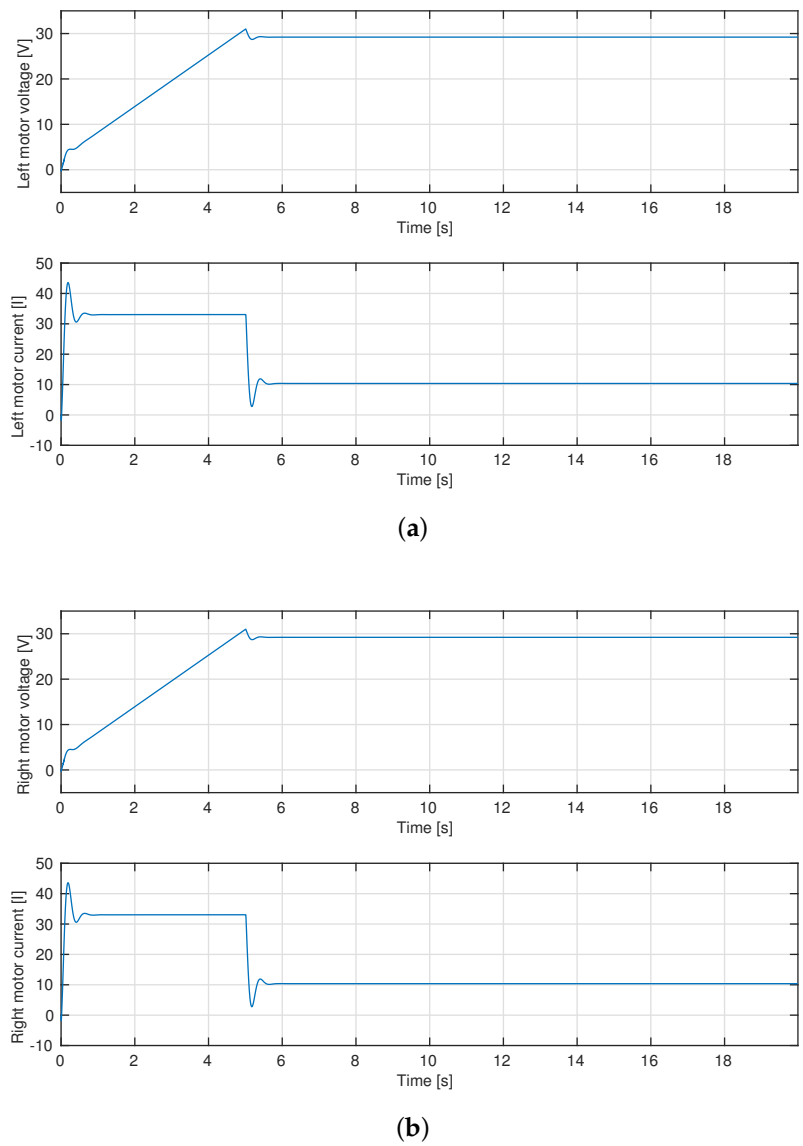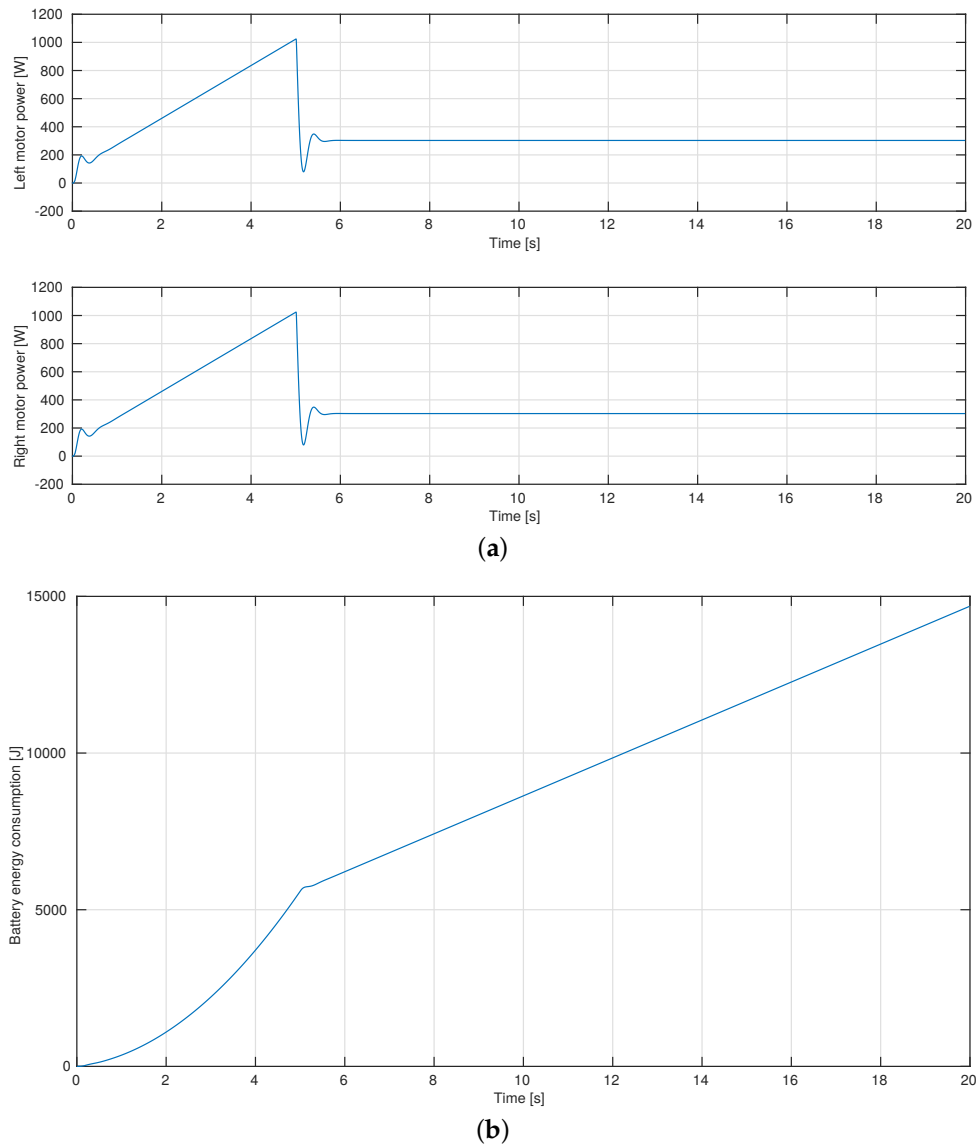


**(a)**



**(b)**

**Figure 11.** Rear in-wheel motor voltage and current. (**a**) Left motor; (**b**) right motor.

**Figure 12.** Rear in-wheel motor power and battery energy consumption. (**a**) Motor power; (**b**) battery energy.

### 4.3. Exploring an Agricultural Field

This second simulation aims at showing the behavior of the robot going back and forth in an agricultural field (Figure 13). The trajectory has a length of 1206.3 m, lasts 300 s and lays out over a plane with slope 45°, the maximum slope the robot can traverse without facing rollover issues.

Figure 14a shows the mechanical torque time history. In this case, the maximum value is less than 6 Nm, appearing when the vehicle reaches the maximum speed (Figure 14b). When it happens, the vehicle starts to decelerate until its speed is near zero at the end of the curve, making the turn easier and preventing the motors from feed torques above the nominal value. As the vehicle follows this behavior in each curve, the torque exhibits an alternating profile around a positive constant value.

During the execution of the trajectory, motor torques do not exceed the nominal value, confirming the validity of the design. This implies that motor voltages and currents (Figure 15) are below the maximum values, as well.
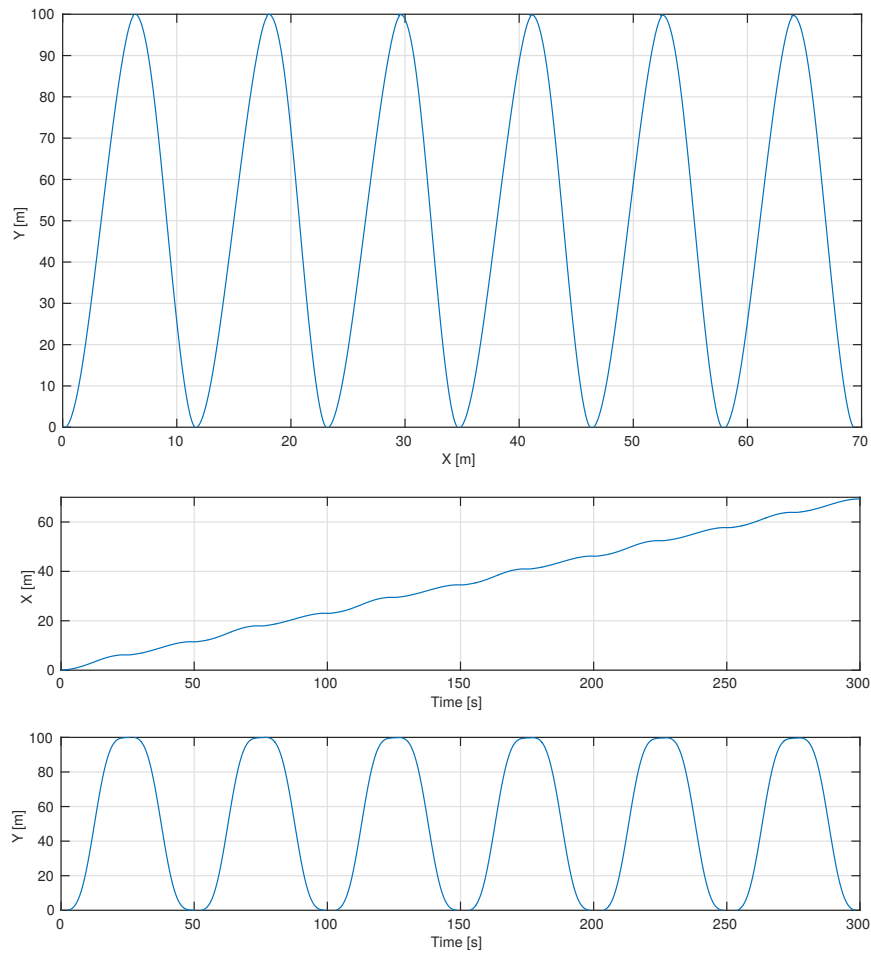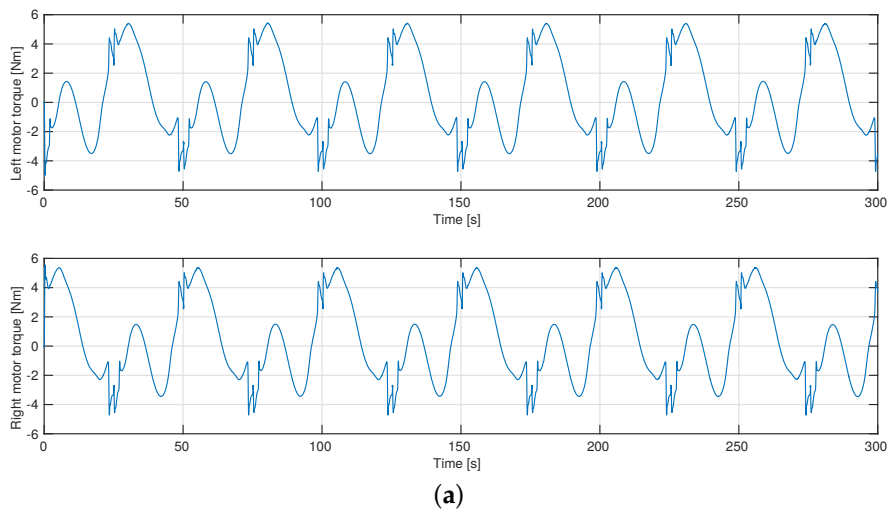
**Figure 13.** Trajectory of the robot in the *xy* plane.
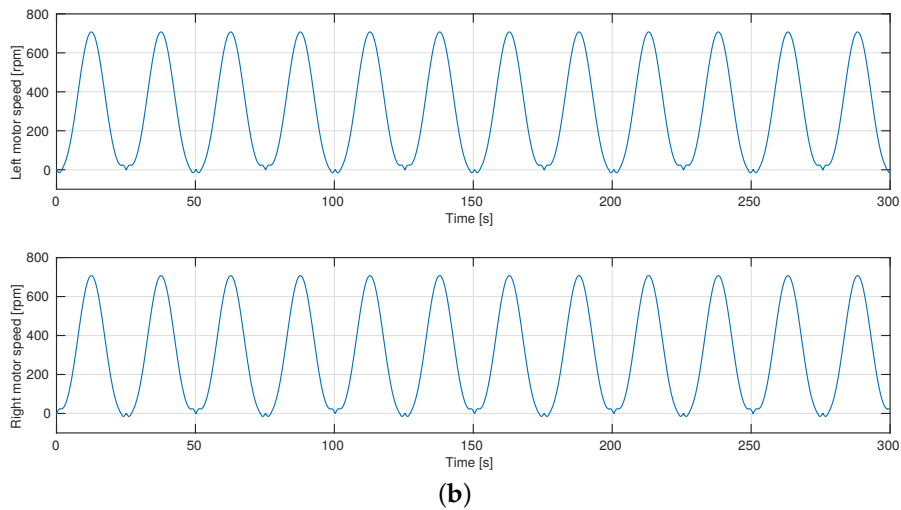
(**a**)

**Figure 14.** *Cont.*

**Figure 14.** Torque and speed of the rear left and right in-wheel motors. (**a**) Motor torque; (**b**) motor speed.
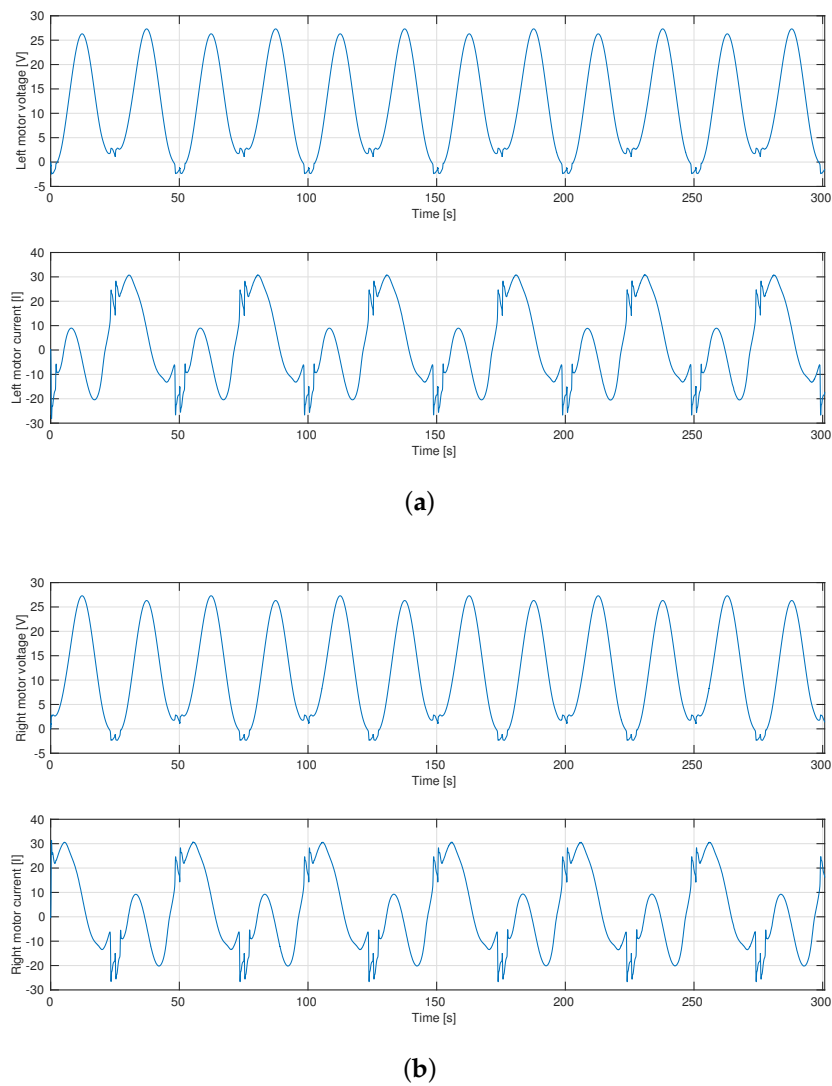


(**a**)



(**b**)

**Figure 15.** Rear in-wheel motor voltage and current. (**a**) Left motor; (**b**) right motor.

Finally, Figure 16 shows the motor power of rear motors and the battery energy consumption. The energy required to execute the trajectory at the conditions considered in this simulation is approximately 14.7 Wh. Considering that the battery pack has a capacity of 972 Wh, the vehicle autonomy in this situation is approximately 5 h 31 min.
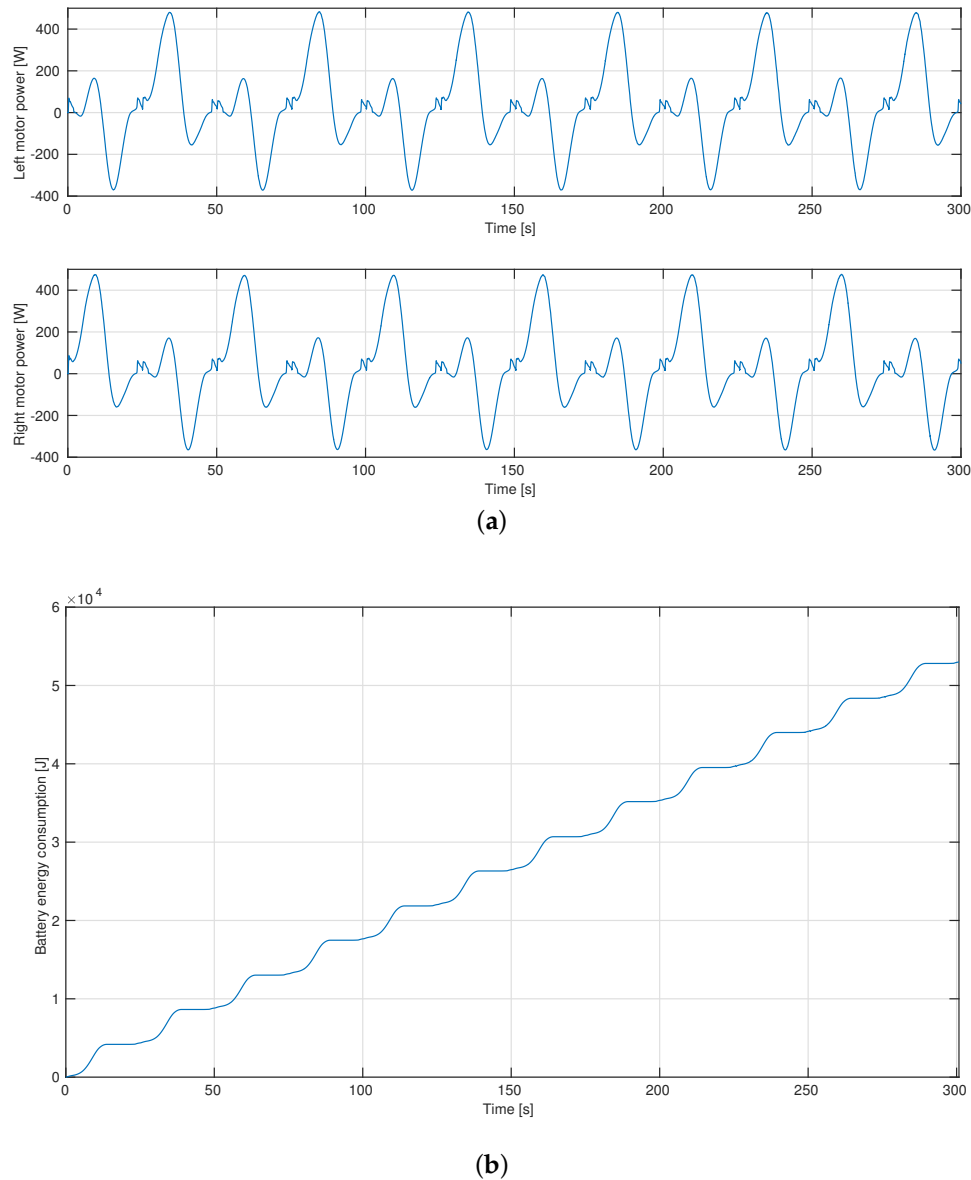
**Figure 16.** Rear in-wheel motor power and battery energy consumption. (**a**) Motor power; (**b**) battery energy.

## 5. Conclusions

This paper describes the design of ROBI′, a prototype mobile manipulator for agricultural applications. The mechanical design and the selection of the motion control system devices, aiming at low cost, low weight, simplicity and modularity, are presented.

A model of the robot, suitable for the preliminary simulations required to verify the design, especially in terms of motor power and battery pack capacity, is also derived, including an experimental characterization of the in-wheel motors.

Finally, two simulations, one related to a realistic agricultural trajectory, show the behavior of the most important electrical and mechanical quantities, confirming the validity of the robot design.

The model here presented will be used, in the near future, to develop the robot control system and to design innovative electrical agricultural tools. Figure 17 shows an example of the design of a mechanical weeder that can be mounted on ROBI'.
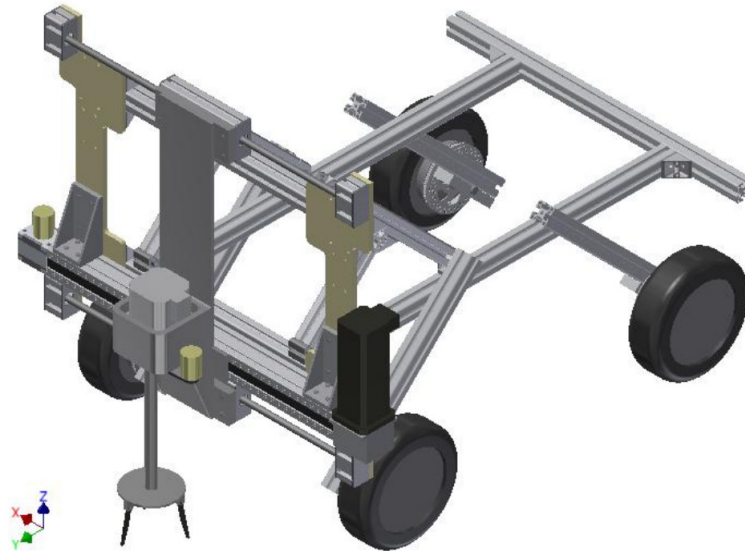


**Figure 17.** A 3D rendering of a possible future development.

**Author Contributions:** All the authors equally contributed to the work.

**Conflicts of Interest:** The authors declare no conflict of interest.

## References

1. Herring, D. Precision Farming: Feature Articles. *NASA Earth Obs.* 29 January 2001. Available online: https://earthobservatory.nasa.gov/Features/PrecisionFarming/ (accessed on 14 March 2017).
2. Cucci, D.; Matteucci, M. On the development of a generic multi-sensor fusion framework for robust odometry estimation. *J. Softw. Eng. Robot.* **2014**, *5*, 48–62.
3. Cucci, D.; Matteucci, M.; Bascetta, L. Pose tracking and sensor self-calibration for an all-terrain autonomous vehicle. In *IFAC-PapersOnLine, Prodceedings of 9th IFAC Symposium on Intelligent Autonomous Vehicles IAV 2016, Leipzig, Germany, 29 June—1 July 2016*; Springer: Berlin/Hedelberg, Germany, 2016; Volume 49, pp. 25–31.
4. Tahirović, A.; Magnani, G. General framework for mobile robot navigation using passivity-based MPC. *IEEE Trans. Autom. Control* **2011**, *56*, 184–190.
5. Tahirović, A.; Brkić, M.; Magnani, G.; Bascetta, L. A planner for All-Terrain Vehicles on unknown rough terrains based on the MPC paradigm and D\*-like algorithm. In Proceedings of the IEEE International Conference on Robotics and Automation, Workshop on Modelling, Estimation, Perception and Control of All Terrain Mobile Robots, Hong Kong, China, 1 June 2014.
6. Bascetta, L.; Cucci, D.; Matteucci, M. Kinematic trajectory tracking controller for an all-terrain Ackermannn steering vehicle. In *IFAC-PapersOnLine, Prodceedings of 9th IFAC Symposium on Intelligent Autonomous Vehicles IAV 2016, Leipzig, Germany, 29 June—1 July 2016*; Springer: Berlin/Hedelberg, Germany, 2016; Volume 49, pp. 13–18.
7. D'Amelio, E.; Bascetta, L.; Cucci, D.; Matteucci, M.; Bardaro, G. A Modelica simulator to support the development of the control system of an autonomous All-Terrain mobile robot. In *IFAC-PapersOnLine, Proceedings of the Vienna Conference on Mathematical Modelling, Vienna, Austria, 18–20 February 2015*; Springer: Berlin/Hedelberg, Germany, 2015; Volume 48, pp. 274–279.
8. Bardaro, G.; Cucci, D.; Bascetta, L.; Matteucci, M. A simulation based architecture for the development of an autonomous all terrain vehicle. In Proceedings of the Simulation, Modeling, and Programming for Autonomous Robots—Lecture Notes in Computer Science, Bergamo, Italy, 20–23 October 2014; pp. 74–85.

9.    Edan, Y.; Miles, G. Systems engineering of agricultural robot design. *IEEE Trans. Syst. Man Cybern.* **1994**, *24*, 1259–1265.

10.   Chatzimichali, A.; Georgilas, I.; Tourassis, V. Design of an advanced prototype robot for white asparagus harvesting. In Proceedings of the IEEE/ASME International Conference on Advanced Intelligent Mechatronics, Singapore, 14–17 July 2009; pp. 887–892.

11.   Feng, Q.; Wang, X.; Wang, G.; Li, Z. Design and Test of Tomatoes Harvesting Robot. In Proceedings of the IEEE International Conference on Information and Automation, Lijiang, Yunnan, China, 8–10 August 2015; pp. 949–952.

12.   Yaguchi, H.; Nagahama, K.; Hasegawa, T.; Inaba, M. Development of an Autonomous Tomato Harvesting Robot with Rotational Plucking Gripper. In Proceedings of the IEEE/RSJ International Conference on Intelligent Robots and Systems, Daejeon, Korea, 9–14 Octorber 2016; pp. 652–657.

13.   Gonzalez-de-Santos, P.; Ribeiro, A.; Fernandez-Quintanilla, C.; Lopez-Granados, F.; Brandstoetter, M.; Tomic, S.; Pedrazzi, S.; Peruzzi, A.; Pajares, G.; Kaplanis, G.; et al. Fleets of robots for environmentally-safe pest control in agriculture. *Precis. Agric.* **2016**, 1–41, doi:10.1007/s11119-016-9476-3.

14.   Grimstad, L.; Pham, C.; Phan, H.; From, P. On the design of a low-cost, light-weight, and highly versatile agricultural robot. In Proceedings of the IEEE International Workshop on Advanced Robotics and Its Social Impacts, Lyon, France, 30 June–2 July 2015.

15.   Roshanianfard, A.; Noguchi, N. Development of a 5DOF robotic arm (RAVebots-1) applied to heavy products harvesting. In *IFAC-PapersOnLine, Proceedings of 5th IFAC Conference on Sensing, Control and Automation Technologies for Agriculture AGRICONTROL 2016, Seattle, WA, USA, 14—17 August 2016*; Springer: Berlin/Hedelberg, Germany, 2016; Volume 49, pp. 155–160.

16.   Wang, G.; Yu, Y.; Feng, Q. Design of End-effector for Tomato Robotic Harvesting. In *IFAC-PapersOnLine, Proceedings of 5th IFAC Conference on Sensing, Control and Automation Technologies for Agriculture AGRICONTROL 2016, Seattle, WA, USA, 14–17 August 2016*; Springer: Berlin/Hedelberg, Germany, 2016; Volume 49, pp. 190–193.

17.   Levin, M.; Degani, A. Design of a Task-Based Modular Re-Configurable Agricultural Robot. In *IFAC-PapersOnLine, Proceedings of 5th IFAC Conference on Sensing, Control and Automation Technologies for Agriculture AGRICONTROL 2016, Seattle, WA, USA, 14–17 August 2016*; Springer: Berlin/Hedelberg, Germany, 2016; Volume 49, pp. 184–189.

18.   Hanhui, L.; Ken, C.; Huazhou, C.; Zhaofeng, Z. Optimization design of fruit picking end-effector based on its grasping model. *INMATEH-Agric. Eng.* **2014**, *47*, 81–90.

19.   Ryoo, Y.J.; Lee, K.N.; Choi, P.G. Intelligent Platform Design of Agricultural Robot Inspired by Farmer Assistance (AGRIFA). In Proceedings of the Joint International Conference on Soft Computing and Intelligent Systems, and International Symposium on Advanced Intelligent Systems, Kobe, Japan, 20–24 November 2012; pp. 2037–2039.

20.   Corpe, S.; Tang, L.; Abplanalp, P. GPS-Guided Modular Design Mobile Robot Platform for Agricultural Applications. In Proceedings of the 7th International Conference on Sensing Technology, Wellington, New Zealand, 3–5 December 2013; pp. 806–810.

21.   Durmuş, H.; Güneş, E.; Kirci, M.; Üstündağ, B. The design of general purpose autonomous agricultural mobile-robot: "AGROBOT". In Proceedings of the International Conference on Agro-Geoinformatics (Agro-geoinformatics), Istanbul, Turkey, 20–24 July 2015.

22.   Ko, M.; Ryuh, B.S.; Kim, K.; Suprem, A.; Mahalik, N. Autonomous Greenhouse Mobile Robot Driving Strategies From System Integration Perspective: Review and Application. *IEEE/ASME Trans. Mechatron.* **2015**, *20*, 1705–1716.

23.   Hassan, M.; Ullah, M.; Iqbal, J. Towards autonomy in agriculture: Design and prototyping of a robotic vehicle with seed selector. In Proceedings of the International Conference on Robotics and Artificial Intelligence, Rawalpindi, Pakistan, 1–2 November 2016; pp. 37–44.

24.   Bechar, A.; Vigneault, C. Agricultural robots for field operations: Concepts and components. *Biosyst. Eng.* **2016**, *149*, 94–111.

25.   Bechar, A.; Vigneault, C. Agricultural robots for field operations. Part 2: Operations and systems. *Biosyst. Eng.* **2017**, *153*, 110–128.

26.   Bloch, V.; Bechar, A.; Degani, A. Development of an environment characterization methodology for optimal design of an agricultural robot. *Ind. Robot Int. J.* **2017**, *44*, 94–103.

27. Bogue, R. Robots poised to revolutionise agriculture. *Ind. Robot Int. J.* **2016**, *43*, 450–456.

28. *ISO 17396:2014: Synchronous Belt Drives—Metric Pitch, Trapezoidal Profile Systems T and AT, Belts and Pulleys*; Technical Report; International Organization for Standardization: Geneva, Switzerland, January 2014.

29. VESC—Open Source ESC. Available online: http://vedder.se/2015/01/vesc-open-source-esc (accessed on 14 January 2017).

30. Cook, G. *Mobile Robots: Navigation, Control and Remote Sensing*; John Wiley & Sons: Hoboken, NJ, USA, 2011.

31. Pacejka, H. The magic formula tire model. *Veh. Syst. Dyn.* **1992**, *21*, 1–18.

32. Pacejka, H. *Tire and Vehicle Dynamics*; Elsevier: Amsterdam, The Netherlands, 2005.